Check for updates

# Calculation of critical nucleation rates by the persistent embryo method: application to quasi hard sphere models

Shang Ren, [ID] [ab] Yang Sun, [ID] *[b] Feng Zhang,*[b] Alex Travesset, [ID] [ab]
Cai-Zhuang Wang[ab] and Kai-Ming Ho[abc]

We study the crystal nucleation of the Weeks–Chandler–Andersen (WCA) model, using the recently introduced persistent embryo method (PEM). The method provides detailed characterization of pre-critical, critical and post-critical nuclei, as well as nucleation rates that compare favorably with those obtained using other methods (umbrella sampling, forward flux sampling or seeding). We further map our results to a hard sphere model allowing comparison with other existing predictions. Implications for experiments are also discussed.

## 1. Introduction

The nucleation of a crystal out of a supercooled fluid is a fundamental process of enormous complexity. Even though classical nucleation theory (CNT) was proposed almost a century ago,[1] it is only recently, with the development of powerful computers, that parameter-free predictions have become possible. Hard sphere (HS) models[2,3] and other closely related systems[4–8] have provided fertile test grounds on which implementations of CNT can be tested: brute force Brownian dynamics (BD),[4,5] forward flux sampling (FFS),[2,4,6] umbrella sampling (US),[4] metadynamics and seeding methods.[7] Despite their obvious theoretical motivations, these models are also of considerable experimental interest, as they approximately describe colloidal dispersions.[9–11] Experimental nucleation rates, however, remain in significant disagreement with most of the existing theoretical predictions using these simple models.[4,12]

Recently, we have introduced the persistent embryo method (PEM)[13] and applied it to the investigation of the nucleation of pure Ni and binary CuZr by all atom MD simulations. In this paper, we demonstrate that PEM is an efficient method by applying it to the Weeks–Chandler–Andersen (WCA) model,[14] assuming the validity of CNT. As we describe further below, PEM can measure the nucleation rate in the low-density regime and does not make any geometrical assumptions on the shape

of the nucleus. Moreover, PEM can obtain the unbiased configuration of the critical nucleus. We expect that PEM will become the method of choice as the optimal implementation of CNT for certain problems. Furthermore, given the current disagreements between nucleation rates as measured in experiments or calculated by theory, new techniques are crucial, in that they provide additional insights on the origins of such discrepancies.

This paper is organized as follows: in Section 2, we present the WCA model, including the description of Brownian dynamics and order parameter. In Section 3, we show the method and discuss the calculation of other necessary quantities, such as the chemical potential. Section 4 describes the persistent embryo method (PEM) and Section 5 describes the determination of attachment rate. In Section 6, we derive the rate equation and present our predictions. In Section 7, we discuss our results and compare them with existing estimates obtained by other methods. A comparison with experimental results is also included. The conclusions are left for Section 8.

## 2. WCA model and simulation details

To relate our calculation to experiments,[9–11] and also to compare with previous computational works,[4–6] we performed Brownian dynamics (BD) simulations of $N$ particles interacting with the WCA potential:[14]

$$U_{\mathrm{WCA}}(r) = \begin{cases} 4\varepsilon\left[\left(\dfrac{\sigma}{r}\right)^{12} - \left(\dfrac{\sigma}{r}\right)^{6} + \dfrac{1}{4}\right] & r \leq 2^{\frac{1}{6}}\sigma \\ 0 & r > 2^{\frac{1}{6}}\sigma \end{cases}$$

[a] Department of Physics and Astronomy, Iowa State University, Ames, Iowa 50011, USA

[b] Ames Laboratory, U.S. Department of Energy, Ames, Iowa 50011, USA.
E-mail: yangsun@ameslab.gov, fzhang@ameslab.gov

[c] Hefei National Laboratory for Physical Sciences at the Microscale and Department of Physics, University of Science and Technology of China, Hefei, Anhui 230026, China

where $\sigma$ is the unit of length and $\varepsilon$ is the unit of energy. The WCA model is a softer version of the HS system,[14] and it is possible to define a mapping from the WCA model to the HS model, as we discuss this further below.

Brownian dynamics is the overdamped limit of Langevin dynamics. In Brownian dynamics, the equation of motion of particle $i$ is:

$$\frac{d\boldsymbol{r}_i}{dt} = \frac{1}{M\gamma}[-\nabla_i U + \boldsymbol{W}_i(t)] \tag{1}$$

where $\gamma$ is the friction coefficient with units of inverse time. $\boldsymbol{W}_i(t)$ is the stochastic force and $M$ is the mass of the particle, which is subject to a conservative force $-\nabla_i U$. The stochastic force is correlated according to the dissipation–fluctuation theorem $\langle \boldsymbol{W}_i(t)\boldsymbol{W}_j(t')\rangle = 6M\gamma k_B T\delta_{ij}\delta(t - t')$, where $\delta$ is the Kronecker delta function and $k_B$ is the Boltzmann constant. The timestep of the simulation is $0.0004\tau$ ($\tau$ is the Lennard-Jones (LJ) time unit which equals $\sqrt{\frac{m\sigma^2}{\varepsilon}}$, where $m$ is the unit of mass).

Note the Brownian time $\tau_B$ is defined as $\tau_B = \frac{\sigma^2}{D}$, where $D$ is the diffusion coefficient on the Brownian motion determined by the Einstein relation $D = k_B T/M\gamma$. Following Kawasaki and Tanaka,[5] we studied the WCA model at the reduced temperature $\beta\varepsilon = 40$, i.e. $T = 0.025\varepsilon/k_B$. For simplicity, both $M$ and $\gamma$ were set to unity. Therefore, $D = 0.025\frac{\sigma^2}{\tau}$ and $\tau_B = 40\tau$. All the simulations were performed using the GPU-accelerated LAMMPS code.[15–17] Some of the results were also tested using HOOMD-blue.[18,19]

Identification of fluid-like and solid-like particles was accomplished by the use of the bond-orientational order parameter,[20,21] which is described below for the sake of completeness. For each particle $i$, the bond-orientational order parameter is:

$$q_{6m}(i) = \frac{1}{N_b(i)} \times \sum_{j=1}^{N_b(i)} Y_{lm}(\vec{r}_{ij}) \tag{2}$$

where $Y_{lm}$ is the spherical harmonics, $\vec{r}_{ij}$ is the position vector of particle $j$ with regard to particle $i$, and $N_b(i)$ is the number of nearest neighbors of particle $i$. The normalized bond-orientational order parameter is:

$$\tilde{q}_{6m}(i) = \frac{q_{6m}(i)}{\left[\sum_{m=-6}^{6} |q_{6m}(i)|^2\right]^{1/2}} \tag{3}$$

A correlation between two particles $(i, j)$ is defined by:

$$S_{ij} = \sum_{m=-6}^{6} q_{6m}(i)q_{6m}^*(j) \tag{4}$$

If $S_{ij}$ exceeds a threshold, then the two particles are considered bonded. To compare with a previous study,[4] we chose $N_b(i)$ as the number of particles within a cutoff of $1.5\sigma$, and a threshold value for $S_{ij}$ of 0.7. We denote $\xi$ as the minimal number of connected neighbors for a particle to be considered as solid. In our simulation, if a given particle has 6 or more connected neighbors, it is considered as a solid-like particle, i.e., $\xi = 6$.

This choice is somewhat arbitrary, and we will show later that it leads to a significant uncertainty in the calculation of related physical quantities, as we explore the cases of $\xi = 8$ and 9, and make an additional comparison with Filion et al.[4]

# 3. Chemical potential differences

The chemical potential difference between solid and fluid ($\Delta\mu$) is required for calculation of nucleation rates by CNT. To compute $\Delta\mu$, we make use of the Gibbs–Helmholtz integration:

$$\frac{\Delta\mu}{T_f} = \int_{T_m}^{T_f} \frac{\Delta H(T)}{T^2}dT \tag{5}$$

where $\Delta H(T)$ is the enthalpy difference between the solid and fluid under the target pressure, $T_m$ is the melting temperature, and $T_f$ is the final target temperature. The $NPT$ ensemble was applied to calculate enthalpy ($H$). For a fixed density, we first ran a BD simulation at the target temperature ($\beta\varepsilon = 40$) to obtain the target pressure $P_f$ in the fluid for subsequent simulations. The target pressure in different densities is presented in Table 1, in the reduced form. To perform the constant pressure simulation for Brownian particles, we used the Berendsen barostat.[22] We ran separate simulations with 4000 particles in a solid face-centered cubic (FCC) phase and a fluid phase at the same temperature. We considered the FCC phase as it is well established that it has the lowest free energy among all putative crystalline phases in a HS system. Other possibilities, such as body-centered cubic (BCC) and icosahedral phases, do not seem to play a role in the nucleation of a monodisperse HS system.[3] As a cross-check, we ran simulations with a BCC embryo and found that it did not nucleate a crystal (see Appendix B).

To prepare the supercooled fluid phase, we first melted a crystal at a high temperature and cooled it down to the target temperature. The numerical integration was carried out using a chained trapezoidal rule with the interval of temperature $\Delta T = 0.0001\varepsilon/k_B$.

The melting temperature, as a function of fluid density, is the lower limit of Gibbs–Helmholtz integration. To determine the melting point, we ran BD simulation on a solid–fluid interface generated by melting half of the initial crystal (FCC) structure. During the simulation, the periodic boundary condition was applied, and we only allowed the length of the box in the direction perpendicular to the interface to change, resulting in a constant interfacial area and constant normal pressure: the $NP_xAT$ ensemble, with $x$ being the perpendicular direction. A typical configuration of the $NP_xAT$ simulation is shown in Fig. 1. We monitored the length of the simulation cell $L_x$ along

**Table 1** Thermodynamic properties calculated at various reduced densities, including the reduced pressure ($\beta\rho\sigma^3$), melting point ($k_BT_m/\varepsilon$) and reduced chemical potential difference ($\beta|\Delta\mu|$)

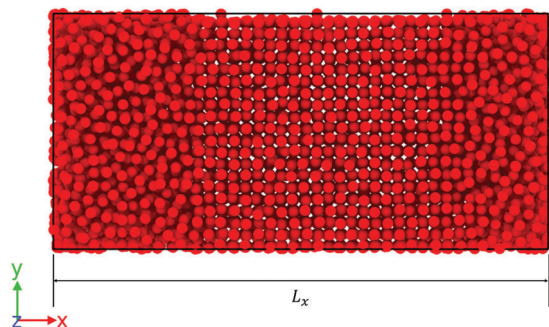| $\rho\sigma^3$ | $\beta p\sigma^3$ | $k_BT_m/\varepsilon$ | $\beta|\Delta\mu|$ |
|---|---|---|---|
| 0.7525 | 11.34 | 0.0318 | 0.3298 |
| 0.7557 | 11.58 | 0.0324 | 0.3591 |
| 0.7588 | 11.83 | 0.0331 | 0.3925 |
| 0.7620 | 12.04 | 0.0337 | 0.4208 |

**Fig. 1** Typical configuration of $NP_xAT$ simulation. The central part is the crystalline phase, while the remaining part is fluid. Periodic boundary conditions were applied during simulation. $L_x$ is the length of the simulation box along the $x$-direction.



**Fig. 3** The reduced chemical potential differences as a function of fluid density. The data from ref. 4 are also included in this figure.

the $x$-direction to locate the phase transition at different temperatures: increasing $L_x$ implies melting and *vice versa*.

A typical measurement of the melting point is exemplified in Fig. 2: at $T = 0.0319\varepsilon/k_B$, the simulation box expands, indicating that the solid is melting towards the fluid. At $T = 0.0317\varepsilon/k_B$, the simulation box shrinks, implying that the fluid side is crystalizing towards the solid. Only at $T = 0.0318\varepsilon/k_B$ does the box size stay around $35.7\sigma$ and both phases coexist. Therefore, this is the melting temperature (within $0.0001\varepsilon/k_B$ precision) at a fluid density $\rho\sigma^3 = 0.7525$. All the melting points thus obtained are shown in Fig. 2(b).

With the measured melting points and enthalpies, we compute the chemical potential differences by eqn (5). A summary of thermodynamic properties is given in Table 1. In Fig. 3, we compared the reduced chemical potential differences with the results from Filion *et al.*,[4] obtained by a thermodynamic integration of the equation of state.[23] Both methods provide consistent results.

## 4. The persistent embryo method (PEM)

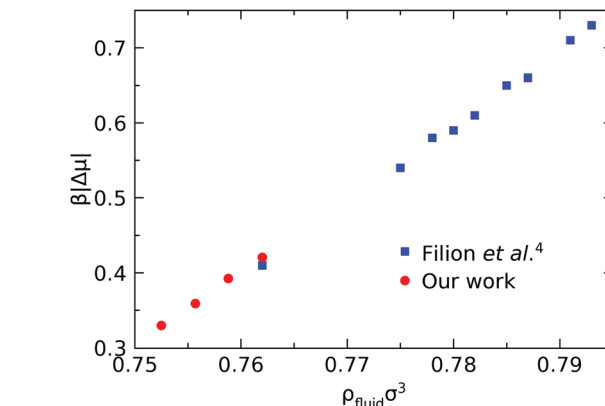Nucleation is described as a competition between the favorable fluid-to-crystal transition and the unfavorable cost to create the solid–fluid interface (SFI), leading to an excess free energy ($\Delta G$):

$$\Delta G(N) = N\Delta\mu + s\left(\frac{N}{\rho}\right)^{\frac{2}{3}}\gamma_i \tag{6}$$

where $\Delta\mu(<0)$ is the chemical potential difference. $\gamma_i(>0)$ is the SFI free energy, and $s$ is a geometric factor that accounts for the possible non-sphericity of the critical nucleus.

During PEM simulation, the number of total particles was set to 13 500. The $NVT$ ensemble was applied during PEM simulation. We first ran a BD simulation for $50\,000\tau_B$ at $\rho\sigma^3 = 0.7525$ and we did not observe a single nucleation event. PEM[13] starts with the creation of a small embryo consisting of a crystal of $N_0$ atoms ($N_0 \ll N^*$), where $N^*$ is the size of the critical nucleus. We inserted this embryo into the supercooled fluid and found that without any other modification, the embryo quickly dissolves back into the fluid. We therefore attached each of the initial embryo particles to a tunable spring while the other end of the spring was fixed to the embryo particle's equilibrium position, so that the embryo is prevented from shrinking and forced to grow. As the embryo grows, springs are gradually softened so that at a size $N_{sc}(<N^*)$, they are completely removed.
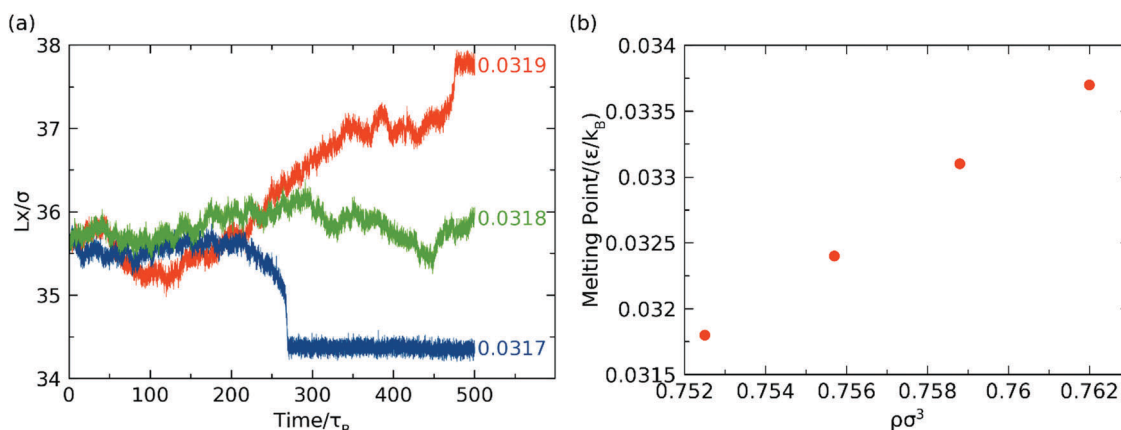


**Fig. 2** (a) $L_x$ as a function of temperature at $T = 0.0317$, $0.0318$, and $0.0319\varepsilon/k_B$. (b) Melting point as a function of reduced density ($\rho\sigma^3$).
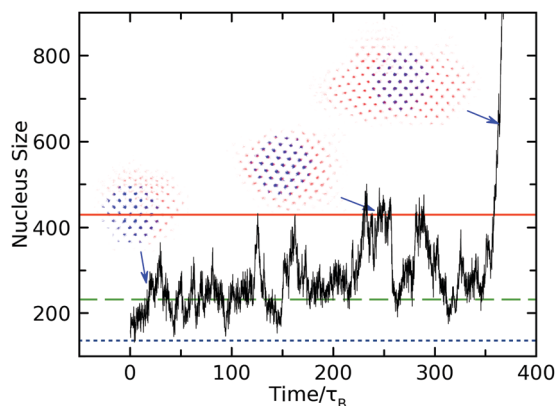
**Fig. 4** Nucleus size *versus* time in the PEM simulation. The dotted line (blue) shows the number of atoms in the embryo ($N_0$), and the dashed line (green) indicates the threshold to remove the springs ($N_{sc}$). The red solid line corresponds to the critical nucleus size ($N^*$), which is determined statistically from 8 plateaus (see Appendix A for the collection). The three insets show the time-averaged shape of pre-critical, critical and post critical nuclei at the corresponding time (arrows). The blue dots indicate the embryo and the red ones are particles attached to the embryo.

This was accomplished by parameterizing the spring constants according to:

$$k(N) = \begin{cases} k_0 \dfrac{N_{sc} - N}{N_{sc}} & \text{if } N < N_{sc} \\ 0 & \text{otherwise} \end{cases} \tag{7}$$

where $N$ is the number of (solid-like) atoms within the nucleus. We ensured that the tunable parameter $N_{sc}$ is much smaller than the critical nucleus size ($N^*$). Some "trial and error" experimentation is needed to determine $N_0$ and $N_{sc}$ if an estimation of $N^*$ is unavailable.

To prepare the sample for our simulation, first, we ran a BD simulation to melt the FCC crystal to a fluid phase. Then, we selected an arbitrary particle as the center and inserted the crystalline embryo (mostly in the FCC phase) into the fluid and deleted the fluid particles that are nearest neighbors to each particle of the initial embryo. During this procedure, we added some crystalline particles into the system while removing the same number of fluid particles, so that the overall density remained constant.

Once the initial configuration was prepared, we started the relaxation of the entire system. First, we fixed the embryo particles and only heated the fluid particles to a relatively high temperature, and then we annealed the fluid particles at high temperature. Finally, we quenched the fluid particles down to the target temperature ($\beta\varepsilon = 40$). This procedure is designed to equilibrate the solid–fluid interface and repel any fluid particles that could be trapped inside the embryo. This preparation process allowed the system to reach thermal equilibrium for further PEM implementation.

We monitored the number of solid-like particles and updated the spring constant every 10 000 steps ($0.1\tau_B$), which we denoted as a loop. At the end of each loop, the size of the crystalline nucleus ($N$) was recalculated, and the spring constant was

**Table 2** Estimates for the nucleus size ($N^*$) and its standard derivation ($\Delta N^*$) and attachment rate ($f^+\tau_B$). $N^*$ and $\Delta N^*$ are calculated in terms of $\xi = 6$, 8 and 9, as shown explicitly

| $\rho\sigma^3$ | $N^* \pm \Delta N^* (\xi = 6)$ | $N^* \pm \Delta N^* (\xi = 8)$ | $N^* \pm \Delta N^* (\xi = 9)$ | $f^+\tau_B$ |
|---|---|---|---|---|
| 0.7525 | $429.76 \pm 26.4$ | $348.06 \pm 21.1$ | $308.89 \pm 18.8$ | 490.7 |
| 0.7557 | $300.67 \pm 20.3$ | $236.13 \pm 19.3$ | $206.09 \pm 18.1$ | 486.9 |
| 0.7588 | $228.30 \pm 14.0$ | $172.85 \pm 10.6$ | $147.65 \pm 9.1$ | 436.4 |
| 0.762 | $190.91 \pm 19.9$ | $141.31 \pm 16.8$ | $118.73 \pm 15.3$ | 437.8 |

updated according to eqn (7). We terminated the simulation if the number of solid-like atoms grew too large (of the order of $5N_{sc}$), as the system was irreversibly crystallized.

The critical nucleus size ($N^*$) was computed by the following algorithm: as shown in Fig. 4, we firstly plotted the embryo size ($N$) *versus* time. According to the CNT, when the size of the nucleus reaches $N^*$, $\Delta G$ reaches a maximum: The nucleus has equal probability to either dissolve or further grow. Therefore, the nucleus size will fluctuate around $N^*$ over a significant period of time, reflected as a plateau in the $N(t)$ time series. To guarantee that the selected plateaus correspond to the critical nucleus, we monitored the height and time width for each plateau. Occasionally, there are sporadic plateaus driven by thermal fluctuations, but those are relatively low and narrow. After a plateau is identified, the average is computed and assigned the critical value $N^*$. We launched many independent simulations (up to 60) to generate significant statistics. A collection of all plateaus is provided in Appendix A. For each plateau, we calculated its average height to cancel out the thermal fluctuation. The critical nucleus size $N^*$ and the standard deviation of the measurement were then determined by averaging the heights of all the plateaus.

Fig. 4 shows a typical PEM simulation, where we show the embryo size *versus* time at $\rho\sigma^3 = 0.7525$. $\xi = 6$ was applied in this case. There are several critical plateaus before the nucleus irreversibly grows. The actual critical nucleus including all the atoms shows a clear anisotropic shape with obvious crystalline facets.

We considered at least 8 plateaus at every density. The averaged critical nucleus size $N^*$ and the standard deviation
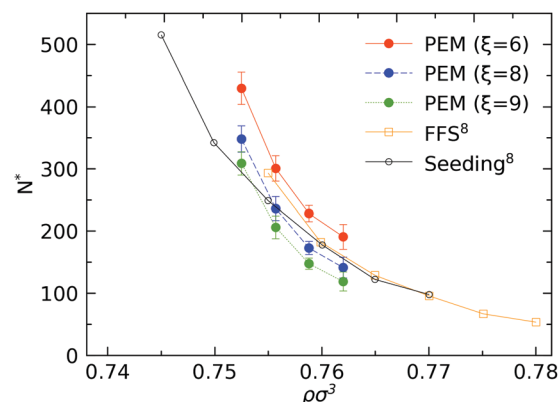


**Fig. 5** Critical nucleus size ($N^*$) as a function of reduced (fluid) density ($\rho\sigma^3$). All the results from $\xi = 6$ (red solid line), $\xi = 8$ (blue dashed line) and $\xi = 9$ (green dotted line) are considered. Previous results are given by either forward flux sampling (FFS) or the seeding method from ref. 8, using $\xi = 9$.
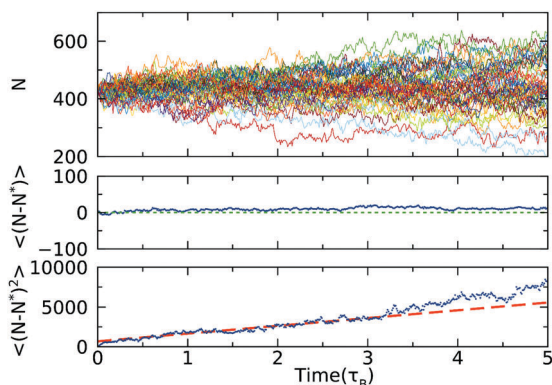
**Fig. 6** The upper panel shows the nucleus size *versus* time for the isoconfigurational ensemble including 50 runs. The middle panel shows the ensemble average of $N^*(t) = N(t) - N^*$. The dotted line (green) serves as a guide to the eye for the zero point. The bottom panel shows the ensemble average of $|N^*(t)|^2 = |N(t) - N^*|^2$. The dashed line (red) indicates the linear fitting to the range from $0.5\tau_B$ to $3\tau_B$ to derive the attachment rate. From $0.5\tau_B$ to $3\tau_B$, $N^*(t)$ remains almost zero.

are summarized in Table 2. A comparison between our result and ref. 8 is given in Fig. 5. Overall, our results of $\xi = 6$ are in better agreement with those obtained by forward flux sampling (FFS)[8] than those from the seeding method.[8] The deviation between the PEM and the seeding method may originate from the geometrical assumption of the critical nucleus in the seeding method. Another comparison between the PEM and the seeding method can be found in the supplementary material of ref. 13. To make a comparison, all the results from $\xi = 6$, 8 and 9 are included in Fig. 5.

## 5. Attachment rate

The attachment rate at the critical nucleus was calculated using the method first introduced by Auer and Frenkel.[24] It considers the size change of the critical nucleus, based on the iso-configurational ensemble,[25] which is given by the formula:

$$f^+ = \frac{\left\langle |N(t) - N^*|^2 \right\rangle}{2t} \tag{8}$$

To determine the attachment rate, we selected a snapshot from PEM simulations whose nucleus size is exactly $N^*$ as the initial configuration. We then performed 50 independent runs starting from this configuration. Different trajectories were reached in these runs because of the random noise introduced by reinitializing the random force term $\mathbf{W}(t)$ in the Langevin equation for each particle. (The springs are absent.)

Fig. 6 shows a determination of attachment rates at $\rho\sigma^3 = 0.7525$. From the upper panel, we notice that roughly half of the runs ended up melting back into the fluid, while the other half grew irreversibly, as expected. Further confirmation was obtained by plotting the ensemble average $\Delta N^*(t) = N(t) - N^*$. According to the CNT, $\frac{d\langle \Delta N^*(t) \rangle}{dt} = 0$ at $N^*$, which is clearly shown in Fig. 6. Therefore, we can measure the attachment rate

**Table 3** Mapped volume fraction ($\phi_{\text{eff}}$, see below for its definition) and nucleation rate ($J\sigma^5/D$) as a function of reduced density ($\rho\sigma^3$). Nucleation rate was calculated in the cases of $\xi = 6$, 8 and 9

| $\rho\sigma^3$ | $\phi_{\text{eff}}$ | $J\sigma^5/D$ ($\xi = 6$) | $J\sigma^5/D$ ($\xi = 8$) | $J\sigma^5/D$ ($\xi = 9$) |
|---|---|---|---|---|
| 0.7525 | 0.5200 | $3.934 \times 10^{-31}$ | $3.103 \times 10^{-25}$ | $2.104 \times 10^{-22}$ |
| 0.7557 | 0.5222 | $1.051 \times 10^{-23}$ | $1.280 \times 10^{-18}$ | $1.917 \times 10^{-16}$ |
| 0.7588 | 0.5243 | $1.097 \times 10^{-19}$ | $6.715 \times 10^{-15}$ | $1.022 \times 10^{-12}$ |
| 0.762 | 0.5265 | $1.294 \times 10^{-17}$ | $5.120 \times 10^{-13}$ | $2.185 \times 10^{-11}$ |

by fitting the slope of $|\Delta N^*(t)|^2$ to eqn (8). The obtained attachment rates for different densities are summarized in Table 2.

## 6. Nucleation rate

The nucleation rate $J$ is given by:

$$J = \kappa \exp\left(-\frac{\Delta G^*}{k_B T}\right) \tag{9}$$

where $\kappa$ is a kinetic prefactor. $\Delta G^*$ depends on the driving force $|\Delta\mu|$ and the critical nucleus size $N^*$ by:[13]

$$\Delta G^* = \frac{1}{2}N^*|\Delta\mu| \tag{10}$$

The explicit formula for the nucleation rate is ref. 26

$$J = \rho_L f^+ \sqrt{\frac{|\Delta\mu|}{6\pi k_B T N^*}} \exp\left(-\frac{|\Delta\mu|N^*}{2k_B T}\right) \tag{11}$$

Nucleation rates were computed from eqn (11) and are summarized in Table 3. With nucleation rates of the order of $10^{-15}$ or even smaller, it is not surprising that no nucleation events were observed by brute-force simulation alone.

One should notice that the rate $J$ depends on $N^*$ exponentially, so a small uncertainty in $N^*$ will result in a significant variation in $J$. Our calculation in terms of $\xi = 6$, 8 and 9 reconfirms this statement. It is worth mentioning that PEM rigorously identifies the configuration of the critical nucleus. The error only enters in the identification of the number of solid-like particles. Further discussion about the order parameter can be found in ref. 27–29.
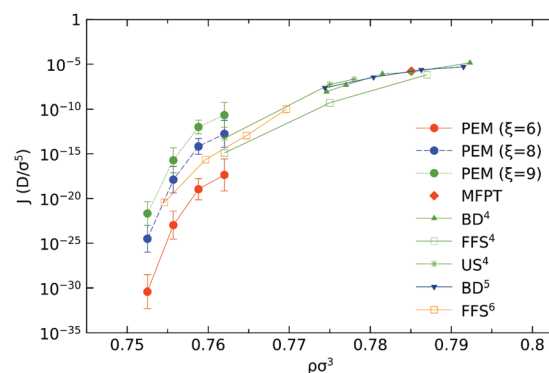


**Fig. 7** The nucleation rate as a function of fluid density, in the cases of $\xi = 6$, 8 and 9. The results from previous work on WCA particles from ref. 4–6 are also included.

# 7. Discussion

Computed nucleation rates are compared to other available estimates in Fig. 7. At a density of $\rho\sigma^3 = 0.762$, the nucleation rates given by Filion *et al.*[4] using US and FFS are in agreement (within the error bar) with our PEM estimates. At the smaller density, PEM gives a slightly lower nucleation rate than FFS from ref. 6. One should notice that the PEM calculations used the *NVT* ensemble, while US and FFS in ref. 4 operated in the *NPT* ensemble. As shown in Table 3, the critical nucleus size at the density of $\rho\sigma^3 = 0.762$ is $N^* = 190.91$, while the total particle number of the system is 13 500. When the nucleus reaches the critical size ($N^*$), it is only 1% of the entire system. In this case, the fluctuations that differentiate the *NVT* and *NPT* ensembles are virtually negligible.[5] In *NVT* simulations, there is a feedback mechanism in that a growing crystalline nucleus has a higher density and thus reduces the overall pressure, which prevents it from growing any further. Thus, the *NVT* simulation actually evaluates the lower limit of the nucleation rates, as compared to the *NPT* case. The influence of order parameter is explicitly shown in Fig. 5, and we will discuss it below. Besides, there is a recent paper[30] that reveals that although FFS is not sensitive to order parameter, the conventional FFS sometimes still underestimates the nucleation rate by several orders of magnitude.

Furthermore, we also measured the nucleation rate at large densities where the nucleation can be directly accessed by brute-force Brownian dynamics simulations. Mean-first passage time[31] was measured from 20 brute-force simulations. The computed nucleation rate is also shown in Fig. 7, which is in good agreement with existing estimates.

To translate the computed nucleation rates of the WCA model to those of HS models, we map the density $\rho$ to the volume fraction $\phi$ by:

$$\phi = \left(\frac{\pi}{6}\right)\rho d^3 \qquad (12)$$

where $d$ is the effective diameter of WCA particles. Here, we follow the same procedure as described by Filion *et al.*[4] to map the freezing density $\rho_f\sigma^3 \simeq 0.712$ of WCA particles to the freezing volume fraction $\phi_F^{HS}$ of hard spheres. Even for the ideal HS model, there is some uncertainty about the exact value of the freezing volume fraction, which is only accurately determined within a range of $0.491 < \phi_F^{HS} < 0.494$.[23,32,33] In our study, we choose $\phi_F^{HS} \simeq 0.492$, as this seems to be the most precise value.[23] Thus, density and volume fraction are related by the effective diameter $d \simeq 1.097\sigma$. The mapped volume fraction is presented in Table 3. Note that while the uncertainty in $\phi_F^{HS}$ appears to be quite small, it may result in a very large dispersion when mapping the number density to the volume fraction. In Fig. 8, the nucleation rates are shown as a function of volume fraction and compared to both experimental and other simulation results. The horizontal error bar indicates the lower and upper limit for volume fractions. Given the logarithmic nature of the plot, slight differences in the mapping result in large shifts of the nucleation rates. Another crucial
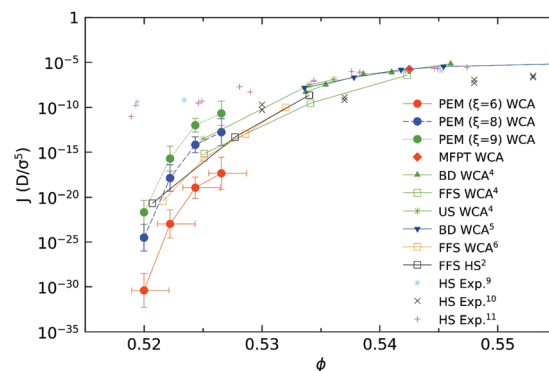


**Fig. 8** Nucleation rates as a function of mapped volume fraction for $\xi = 6$ (red solid line), $\xi = 8$ (blue dashed line) and $\xi = 9$ (green dotted line). Simulation resulting from WCA models,[4–6] hard spheres[2] and experiments[9–11] is included in the figure. The horizontal error bar when $\xi = 8$ and 9 is the same as the case when $\xi = 6$.

factor is the order parameter, as indicated in Fig. 5, 7 and 8. A small change in $\xi$ can lead to a significant change in critical nucleus size ($N^*$) and consequently, the nucleation rate ($J$). But, the advantage of PEM is that it can get the exact configuration of the critical nucleus, while the error is introduced in the counting of solid-like particles. Considering that $J$ relies on $N^*$ exponentially, a small difference of $N^*$ can cause a huge jump of $J$. Any method, as long as it relies on CNT, suffers from this problem. On the other hand, the bond-orientational order parameter is not the only representation of the solid particles within the nucleus. An alternative option is the $(n,\nu)$ parameter, which incorporates a kinetic theory into the descriptor of the nucleus and can be used to describe the dynamics of a sub-critical nucleus.[34,35]

Despite all these uncertainties, our WCA simulations are in clear agreement with previous estimates.[2,4–6] However, all the computed nucleation rates, including current PEM results, deviate from the experimental measurements.[9–11] As pointed out in ref. 4, this discrepancy is not related to inaccuracies of the theoretical calculation but rather, it reflects a true deficiency of HS and related models to capture the physics of these experimental systems. Our calculations support this conclusion.

# 8. Conclusions

We have measured the chemical potential differences between undercooled WCA fluids and solids by Gibbs–Helmholtz integration. We implemented the persistent embryo method (PEM) to evaluate the nucleation rates at the density of $\rho\sigma^3 = 0.7525$, 0.7557, 0.7588, and 0.762. The rates given by PEM are consistent with the ones available from umbrella sampling (US) and forward flux sampling (FFS). Our PEM method is an efficient method to evaluate nucleation rates and it provides a unique characterization of not only the critical, but the dynamics of the pre-critical and post-critical nuclei. Additionally, estimates obtained within WCA models are in agreement with hard spheres. Our results provide more evidence that the discrepancy
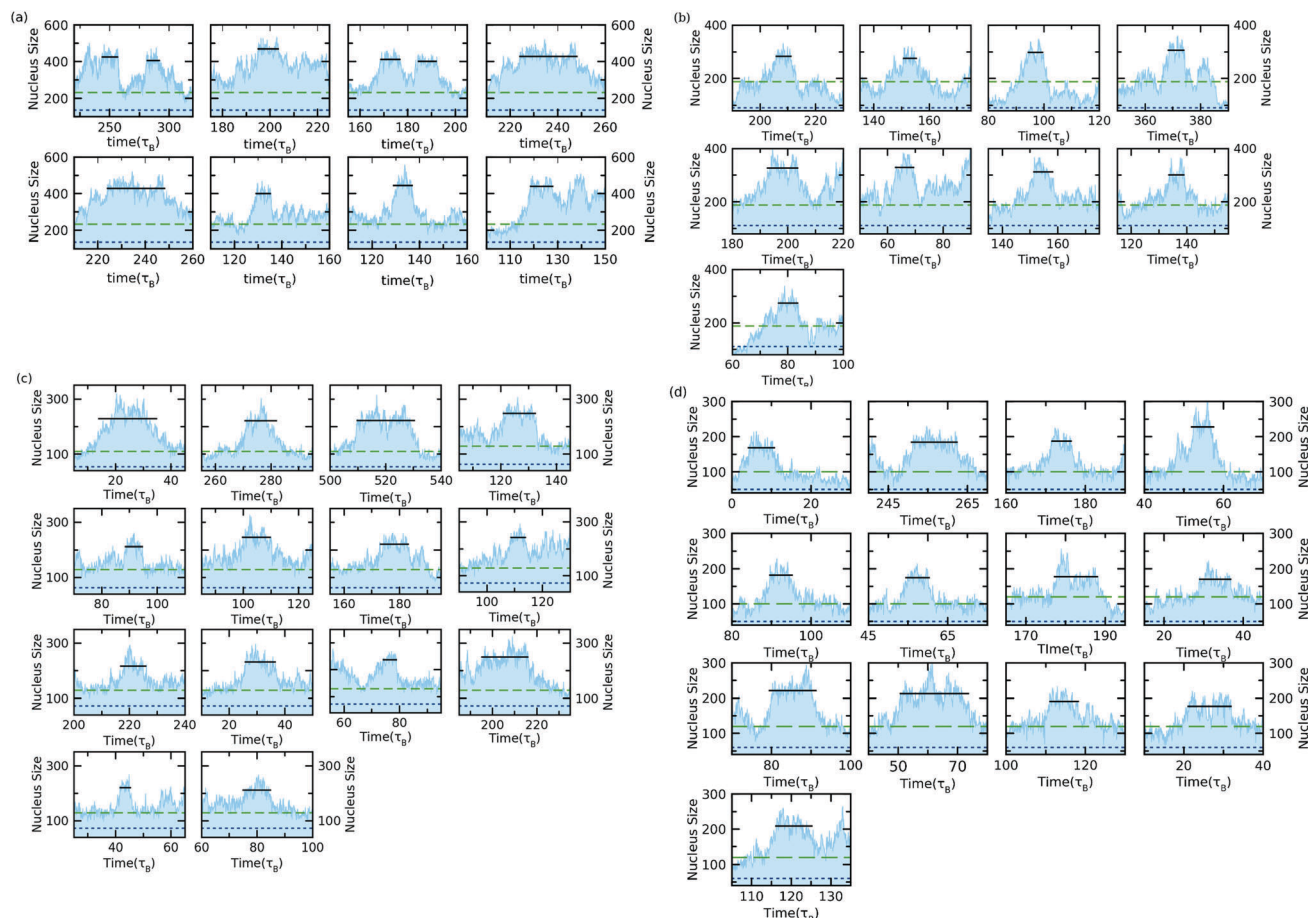
Fig. 9 The plateaus to determine the critical nucleus size at different reduced densities ($\rho\sigma^3$): (a) 0.7525, (b) 0.7557, (c) 0.7588, and (d) 0.762. During the PEM simulation, different $N_0$ values, which is the size of the embryo, and $N_{sc}$ values, which is the threshold where the spin is removed, were applied and indicated by the blue dotted line and green dashed line, respectively. The black solid line shows the averaged height of each plateau.

between simulation and experiments will require more sophisticated models.

## Conflicts of interest

There are no conflicts to declare.

## Appendix A: collection of plateaus

A collection of plateaus is presented in Fig. 9.

## Appendix B: the crystalline and geometrical structure of the embryo

To investigate the effect of the geometry of the embryo, we launched 36 independent PEM simulations under the condition that the embryo is cubic, and 12 plateaus were collected among them. By the same procedure, we find that the critical nucleus size ($N^*$) for $\rho\sigma^3 = 0.7525$ is $303.44 \pm 15.4$, while in the spherical embryo case, $N^* = 300.67 \pm 20.3$. The two ranges have huge overlaps, which indicate that the geometry of the embryo

is not a critical issue in the PEM. A collection of plateaus is presented in Fig. 10.

Besides the geometry, another crucial factor is the structure of the embryo, e.g. how does a BCC embryo work in the PEM? This question was discussed by Auer and Frenkel[3] in the year of 2001. It has been claimed that the BCC and icosahedral geometries do not play a role in the nucleation process of a HS system. To test this, we launched 12 independent runs to justify the effect of the BCC geometry. The result shows that the BCC embryo cannot grow while in the same time period, the FCC embryo can undergo crystallization, as shown in Fig. 11. Therefore, the BCC geometry is not dominant if the nucleus is relatively large, and we excluded the nucleation channel via BCC in our simulation.
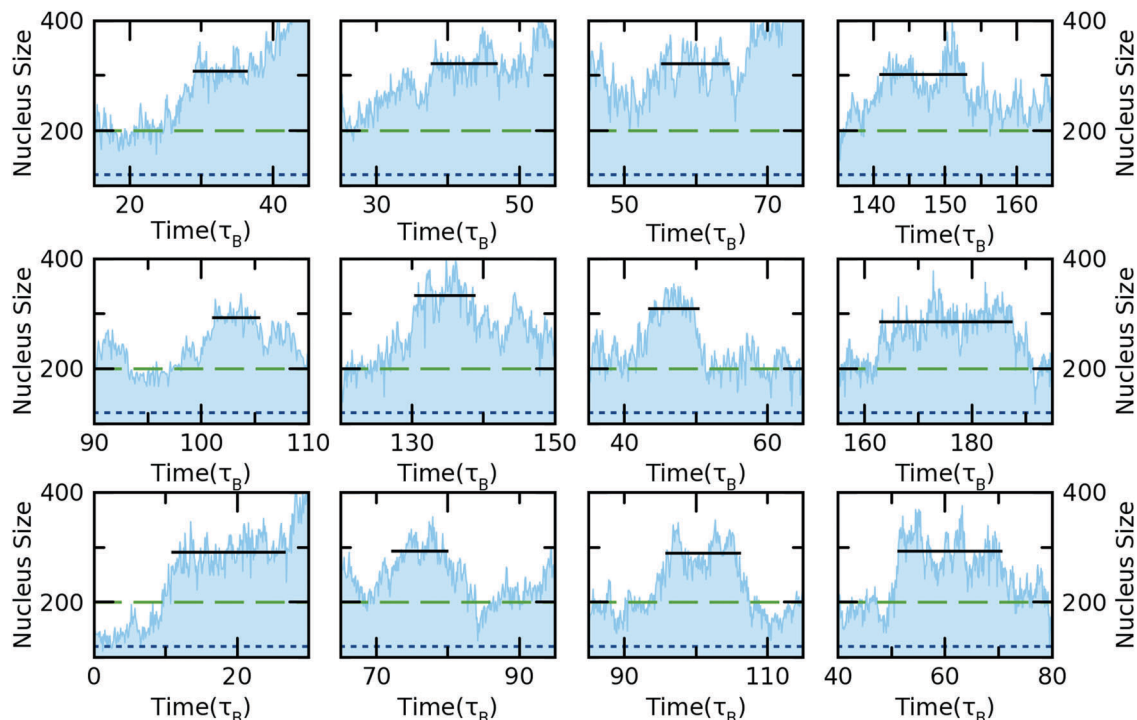
## Acknowledgements

Fig. 10 The plateaus to determine the critical nucleus size in the case of a cubic embryo. The (reduced) density is $\rho\sigma^3 = 0.7557$. During the PEM simulation, different $N_0$ values, which is the size of the embryo, and $N_{sc}$ values, which is the threshold where the spin is removed, were applied and are indicated by the blue dotted line and green dashed line, respectively. The black solid line shows the averaged height of each plateau.
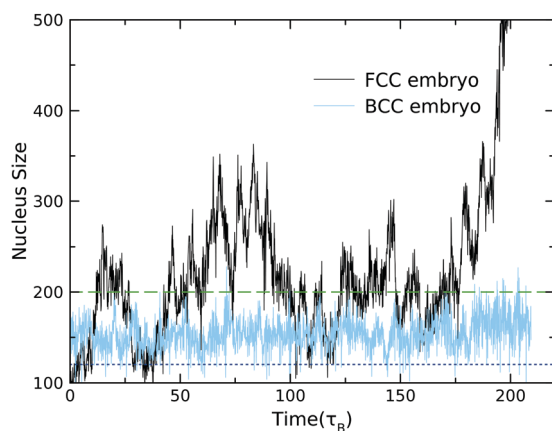


Fig. 11 A comparison of simulations starting with an FCC embryo and BCC embryo. The black line corresponds to the FCC embryo, showing that the FCC embryo eventually grew. The blue line corresponds to the BCC embryo. Within the simulation time, the BCC embryo did not grow.

# References

1 P. Debenedetti, *Metastable liquids: concepts and principles*, Princeton University Press, 1996.

2 L. Filion, M. Hermes, R. Ni and M. Dijkstra, *J. Chem. Phys.*, 2010, **133**, 244115.

3 S. Auer and D. Frenkel, *Nature*, 2001, **409**, 1020–1023.

4 L. Filion, R. Ni, D. Frenkel and M. Dijkstra, *J. Chem. Phys.*, 2011, **134**, 134901.

5 T. Kawasaki and H. Tanaka, *Proc. Natl. Acad. Sci. U. S. A.*, 2010, **107**, 14036–14041.

6 D. Richard and T. Speck, *J. Chem. Phys.*, 2018, **148**, 124110.

7 J. R. Espinosa, C. Vega, C. Valeriani and E. Sanz, *J. Chem. Phys.*, 2016, **144**, 211801.

8 D. Richard and T. Speck, *J. Chem. Phys.*, 2018, **148**, 224102.

9 K. Schätzel and B. J. Ackerson, *Phys. Rev. E: Stat. Phys., Plasmas, Fluids, Relat. Interdiscip. Top.*, 1993, **48**, 3766–3777.

10 J. L. Harland and W. van Megen, *Phys. Rev. E: Stat. Phys., Plasmas, Fluids, Relat. Interdiscip. Top.*, 1997, **55**, 3054–3067.

11 C. Sinn, A. Heymann, A. Stipp and T. Palberg, *Prog. Colloid Polym. Sci.*, Springer Berlin Heidelberg, Berlin, Heidelberg, 2001, vol. 118, pp. 266–275.

12 T. Palberg, *J. Phys.: Condens. Matter*, 2014, **26**, 333101.

13 Y. Sun, H. Song, F. Zhang, L. Yang, Z. Ye, M. I. Mendelev, C. Z. Wang and K. M. Ho, *Phys. Rev. Lett.*, 2018, **120**, 085703.

14 J. D. Weeks, D. Chandler and H. C. Andersen, *J. Chem. Phys.*, 1971, **54**, 5237.

15 W. M. Brown, P. Wang, S. J. Plimpton and A. N. Tharrington, *Comput. Phys. Commun.*, 2011, **182**, 898–911.

16 W. M. Brown, A. Kohlmeyer, S. J. Plimpton and A. N. Tharrington, *Comput. Phys. Commun.*, 2012, **183**, 449–459.

17 W. M. Michael Brown and M. Yamada, *Comput. Phys. Commun.*, 2013, **184**, 2785–2793.

18 J. A. Anderson, C. D. Lorenz and A. Travesset, *J. Comput. Phys.*, 2008, **227**, 5342–5359.

19 J. Glaser, T. D. Nguyen, J. A. Anderson, P. Lui, F. Spiga, J. A. Millan, D. C. Morse and S. C. Glotzer, *Comput. Phys. Commun.*, 2015, **192**, 97–107.

20 P. J. Steinhardt, D. R. Nelson and M. Ronchetti, *Phys. Rev. B: Condens. Matter Mater. Phys.*, 1983, **28**, 784–805.

21 P. Rein ten Wolde, M. J. Ruiz-Montero and D. Frenkel, *J. Chem. Phys.*, 1996, **104**, 9932–9947.

22 H. J. C. Berendsen, J. P. M. Postma, W. F. Van Gunsteren, A. Dinola and J. R. Haak, *J. Chem. Phys.*, 1984, **81**, 3684–3690.

23 D. Frenkel and S. Berend, *Understanding molecular simulation: from algorithms to applications*, Elsevier Science, San Diego, CA, 2001.

24 S. Auer and D. Frenkel, *J. Chem. Phys.*, 2004, **120**, 3015–3029.

25 A. Widmer-Cooper, P. Harrowell and H. Fynewever, *Phys. Rev. Lett.*, 2004, **93**, 135701.

26 K. F. Kelton and A. L. Greer, *Nucleation in Condensed Matter: Applications in Materials and Biology*, Elsevier, Amsterdam, 2010.

27 A. Haji-Akbari and P. G. Debenedetti, *Proc. Natl. Acad. Sci. U. S. A.*, 2015, **112**, 10582–10588.

28 H. Jiang, A. Haji-Akbari, P. G. Debenedetti and A. Z. Panagiotopoulos, *J. Chem. Phys.*, 2018, **148**, 44505.

29 N. E. R. Zimmermann, B. Vorselaars, J. R. Espinosa, D. Quigley, W. R. Smith, E. Sanz, C. Vega and B. Peters, *J. Chem. Phys.*, 2018, **148**, 222838.

30 A. Haji-Akbari, *J. Chem. Phys.*, 2018, **149**, 072303.

31 G. Chkonia, J. Wölk, R. Strey, J. Wedekind and D. Reguera, *J. Chem. Phys.*, 2009, **130**, 64505.

32 R. L. Davidchack and B. B. Laird, *J. Chem. Phys.*, 1998, **108**, 9452–9462.

33 W. G. Hoover and F. H. Ree, *J. Chem. Phys.*, 1968, **49**, 3609–3617.

34 M. J. Uline, K. Torabi and D. S. Corti, *J. Chem. Phys.*, 2010, **133**, 174511.

35 M. J. Uline, K. Torabi and D. S. Corti, *J. Chem. Phys.*, 2010, **133**, 174512.